Annealing behavior of atomic layer deposited HfO_2 films studied by synchrotron x-ray reflectivity and grazing incidence small angle scattering

M. L. Green,[1,a)] A. J. Allen,[1] J. L. Jordan-Sweet,[2] and J. Ilavsky[3]
[1]*National Institute of Standards and Technology, Gaithersburg, Maryland 20899, USA*
[2]*IBM T. J. Watson Research Center, P.O. Box 218, Yorktown Heights, New York 10598, USA*
[3]*Advanced Photon Source, Argonne National Laboratory, Argonne, Illinois 60439, USA*

(Received 26 November 2008; accepted 1 April 2009; published online 28 May 2009)

New results are presented for the annealing behavior of ultrathin complementary-metal-oxide-semiconductor (CMOS) gate dielectric HfO_2 films grown by atomic layer deposition (ALD). A series of ALD HfO_2 dielectric films has been studied by a combination of x-ray reflectivity (XRR) and grazing-incidence small-angle x-ray scattering (GISAXS) measurements. By using these techniques together, we have shown that the surface, interfaces, and internal structure of thin ALD films can be characterized with unprecedented sensitivity. Changes in film thickness, film roughness, or diffuseness of the film/substrate interface as measured by XRR are correlated with the corresponding changes in the internal film nanostructure, as measured by GISAXS. Although the films are dense, an internal film structure is shown to exist, attributed primarily to ≈ 2 nm "missing island" porosity features close to the substrate; these are most likely associated with coalescence defects as a result of initial ALD growth, as they are not observed in the upper regions of the film. Some 8–9 nm heterogeneities are also present, which may indicate a widespread modulation in the film density pervading the entire film volume, and which likely also give rise to surface roughness. Comparison of the data between different scattering geometries and among a carefully designed sequence of samples has enabled important insights to be derived for the annealing behavior of the ALD HfO_2 films. The main effects of single, brief, high temperature excursions to above 900 °C are to anneal out some of the fine voids and reduce the mean roughness and interfacial diffuseness of the film. These changes are indicative of densification. However, depending on the film thickness, the annealing behavior at temperatures between 650 and 800 °C is quite different for single excursion and cyclic anneals. Particularly for thin, just-coalesced films, XRR indicates marked increases in the film thickness and in the mean roughness/diffuseness dimension for cyclic anneals. GISAXS also shows an increase, rather than a reduction, in the void microstructure under these conditions. These changes in the film microstructure appear sufficient to overcome the expected film densification at elevated temperatures with implications for the gate dielectric performance of the films after extended high temperature exposure and cycling, as may occur during gate dielectric fabrication. © *2009 American Institute of Physics*. [DOI: 10.1063/1.3125510]

I. INTRODUCTION

Atomic layer deposition (ALD)[1] is the growth technique of choice for alternate (high-κ) complementary-metal-oxide-semiconductor (CMOS) gate dielectrics[2] as well as other silicon microelectronic applications[3] because it enables the accurate, controlled growth of ultrathin layers. High-κ gate dielectric layers must be ultrathin, planar, and near fully dense in order to minimize their equivalent oxide thickness and thus maximize their capacitance. In this paper, we report the use of x-ray reflectivity (XRR) and grazing-incidence small-angle x-ray scattering (GISAXS) to study the annealing behavior of ALD HfO_2 films. HfO_2 was chosen due to its importance as an alternate gate dielectric to SiO_2.[2,4] After ALD growth, during the thermal budget cycles of the CMOS process flow, the HfO_2 films may densify, oxidize, undergo phase transformations, and/or crystallize, and as a result, affect the electrical performance and reliability of transistor devices.

XRR and GISAXS are powerful techniques for determining changes in film thickness, as well as size and shape of nanostructural features in thin films, as a result of annealing.[5,6] Although GISAXS has been more commonly applied in the quantitative analysis of ordered surface structures or dense packing of islands on surfaces,[7,8] here it is used in the form of conventional small-angle scattering in a grazing-incidence reflection geometry to study the internal microstructure of very thin, dense HfO_2 films. The internal location of this microstructure was first established by varying the incident grazing angle above and below the critical angle. By combining XRR and GISAXS in this way, changes in film thickness and roughness or in the diffuseness of the film/substrate interface (as measured by XRR) can be correlated with the corresponding changes in the internal film microstructure (as measured by GISAXS). In this paper we

[a)]Electronic mail: martin.green@nist.gov.

 © 2009 American Institute of Physics

Author complimentary copy. Redistribution subject to AIP license or copyright, see http://jap.aip.org/jap/copyright.jsp

TABLE I. Annealing treatments given to HfO_2 samples.

Sample	ALD cycles	Thickness (nm)[a]	Annealing temperature °C	Comments
A	25	1.49	350–974	(a) Reflectivity measurements for this annealing series made on the same spot on the same "thin" film
B	60	3.09	350–974	(b) Reflectivity measurements for this annealing series made on the same spot on the same "thick" film
C	25	1.58	300 (reference)	(c) Reflectivity and GISAXS measurements for this annealing series made on separate thin films
D	60	3.46	300 (reference)	(d) Reflectivity and GISAXS measurements for this annealing series made on separate thick films
E	25	1.81	500	(c) Reflectivity and GISAXS measurements for this annealing series made on separate thin films
F	60	2.92	500	(d) Reflectivity and GISAXS measurements for this annealing series made on separate thick films
G	25	1.66	600	(c) Reflectivity and GISAXS measurements for this annealing series made on separate thin films
H	60	3.37	600	(d) Reflectivity and GISAXS measurements for this annealing series made on separate thick films
I	25	1.74	700	(c) Reflectivity and GISAXS measurements for this annealing series made on separate thin films
J	60	3.46	700	(d) Reflectivity and GISAXS measurements for this annealing series made on separate thick films
K	25	1.77	800	(c) Reflectivity and GISAXS measurements for this annealing series made on separate thin films
L	60	3.49	800	(d) Reflectivity and GISAXS measurements for this annealing series made on separate thick films
M	25	1.55	900	(c) Reflectivity and GISAXS measurements for this annealing series made on separate thin films
N	60	2.93	900	(d) Reflectivity and GISAXS measurements for this annealing series made on separate thick films
O	25	1.75	1000	(c) Reflectivity and GISAXS measurements for this annealing series made on separate thin films
P	60	3.30	1000	(d) Reflectivity and GISAXS measurements for this annealing series made on separate thick films

[a]Measured film thicknesses are from reflectivity with an estimated standard deviation uncertainty on each measurement of $\pm$ 0.05 nm. Computed standard deviation uncertainties on the thickness of each coupon are $\pm$0.11 nm for thin films based on samples A, C, E, G, I, K, M, and O and $\pm$0.22 nm for thick films based on samples B, D, F, H, J, L, N, and P (and magnified due to the small thicknesses measured for samples F and N).

describe how this approach has yielded important insights into the annealing behavior of ALD HfO_2 films.

II. EXPERIMENTAL

A. Sample preparation

ALD HfO_2 films were grown on chemically oxidized[9] 200 mm Si (100) wafers. The films were grown at 300 °C using the $HfCl_4/H_2O$ chemistry route. Table I lists the thicknesses of various samples and the annealing treatments to which they were subjected. It is important to note that Table I includes samples subjected to two different annealing conditions: the first comprising one-time brief anneals of different sample coupons to specified annealing temperatures, and the second comprising thermal cycling of the same sample coupon to successively higher annealing temperatures (with cooling to ambient between each anneal). The effect on the microstructure differed significantly between these two annealing conditions, as is discussed in Sec. III.

B. X-ray reflectivity measurements

X-ray specular reflectivity measurements[10,11] were made at beamline X20A at the National Synchrotron Light Source (NSLS), Brookhaven National Laboratory. XRR was employed to determine the mean parallel-sided HfO_2 film thicknesses as well as the corresponding combined film roughness and interfacial diffuseness. These measurements were made in a previously built, custom made annealing chamber that incorporates a computer controlled boron nitride Boralectric[12] heater (Advanced Ceramics Corp., Cleveland, OH), an x-ray transparent Be dome, and gas flowthrough for atmospheric control. Annealing studies were performed using samples (12–15 mm wide, ≈40 mm long) of thin (sample A) and thick (sample B) HfO_2 films. Each sample was heated under a 99.99 mol % He atmosphere to successively higher annealing temperatures (between 350 and 974 °C) held at each temperature for a few minutes, then cooled back to room temperature in He for the reflectivity measurement, which was made on the same area after each anneal. Because the sample was maintained in a single posi-

Author complimentary copy. Redistribution subject to AIP license or copyright, see http://jap.aip.org/jap/copyright.jsp

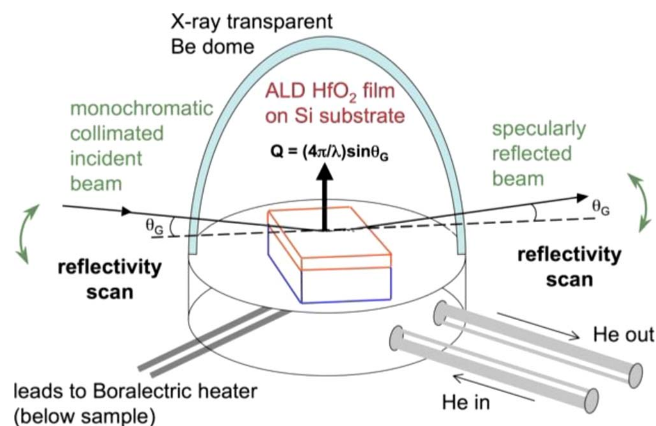

FIG. 1. (Color online) Schematic of x-ray specular reflectivity measurement geometry. Both the incident and reflected grazing angles are θ_G. The beryllium (Be) domed annealing chamber used for *in situ* annealing is also shown.

tion within the annealing chamber for all of the measurements in each case (samples A and B), we denote these as the *in situ* sample results. A nominally identical set of annealed samples (between 500 and 1000 °C in 100° intervals, see Table I) together with unannealed reference samples, were also measured under ambient conditions at X20A. For this set of samples, a different piece (albeit from the same wafer) was used for each annealing temperature. Because the annealing of these samples was carried out prior to the XRR (or GISAXS) measurements, we denote these as the *ex situ* sample results.

The geometry of the XRR experiment is shown in Fig. 1. Si (111) monochromator optics were used to select an incident x-ray energy of 8.046 keV (wavelength=0.1541 nm). Specular reflected intensity was measured with the incident beam collimation and linear detector slits set to equal angles of grazing incidence and specular reflection. The intensity was measured as a function of the incident grazing angle θ_G over the range $0° < \theta_G < 9°$ (detector reflection angle range: $0° < 2\theta_G < 18°$), corresponding to a magnitude Q of the scattering vector $\mathbf{Q}$ perpendicular to the substrate (where $Q = |\mathbf{Q}| = [4\pi/\lambda]\sin\,\theta_G$) in the range $0\ \text{nm}^{-1} < Q < 12.8\ \text{nm}^{-1}$. The angular resolution in θ_G was 0.015° with respect to the sample plane, giving a resolution in Q of $0.021\ \text{nm}^{-1}$. The beam size was 1 mm wide by 0.13 mm high. Consequently, the beam footprint was entirely within the sample area for values of $\theta_G > 0.186°$ (i.e., $Q > 0.26\ \text{nm}^{-1}$). This θ_G is slightly smaller than the critical angle for total reflection θ_c. Based on previous measurements at a higher x-ray energy,[5] we deduce that for the present case $\theta_c = 0.20° \pm 0.05°$ with a corresponding critical $Q_c = 0.28\ \text{nm}^{-1} \pm 0.07\ \text{nm}^{-1}$, where the uncertainties represent estimated standard deviations.

The reflectivity data were analyzed using the well known Parratt model[13] with algorithms derived from the MOTOFIT reflectivity analysis program[14] and implemented as part of the IRENA software package developed by Ilavsky.[15] Some results were also validated using the IMD reflectivity software package[16] used in previous work.[5] Both the mean parallel-sided HfO_2 layer thickness and the roughness and/or interfacial diffuseness were extracted from each reflectivity data

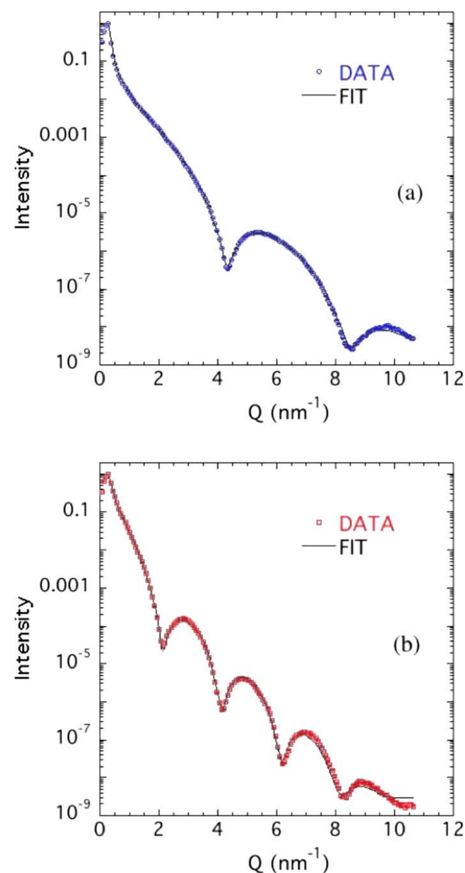

FIG. 2. (Color online) Typical XRR data (open symbols) with computer fits (lines) based on the Parratt model shown for measurements made after an 850 °C anneal for (a) thin and (b) thick films. Uncertainties for individual measurement points are given by the vertical bars, but these are mostly smaller than the symbols themselves. Note the excellent agreement between the data and the model fit.

set. Figure 2 shows the typical reflectivity data with model fits for thin (A) and thick (B) ALD HfO_2 films, each after annealing at 850 °C. Figure 3 presents the deduced x-ray electron density profiles derived from the model fits of Fig. 2. The model determines the roughness/diffuseness dimension σ_R for each of the interfaces as assumed Gaussian standard deviations from their mean positions (the dashed lines). However, as these figures indicate, the true width of each interface (comprised of combined roughness and diffuseness effects) may be better given by $\{2\sigma_R(2\ln 2)^{0.5}\}$, corresponding to a Gaussian full width at half maximum.

C. GISAXS measurements

GISAXS was employed to determine the internal microstructure of the HfO_2 films. Measurements were carried out at sector XOR 8-ID[17,18] at the Advanced Photon Source (APS) at Argonne National Laboratory on samples C–P (Table I). The experimental geometry is shown schematically in Fig. 4. In principle, for the grazing incidence geometry, variation in the scattering intensity with the component of $\mathbf{Q}$ parallel to the substrate $\mathbf{q_y}$ provides in-plane structural information, while the corresponding intensity variation with the $\mathbf{Q}$ component perpendicular to the substrate $\mathbf{q_z}$ provides out-of-plane structural information. In practice, the variations of

Author complimentary copy. Redistribution subject to AIP license or copyright, see http://jap.aip.org/jap/copyright.jsp

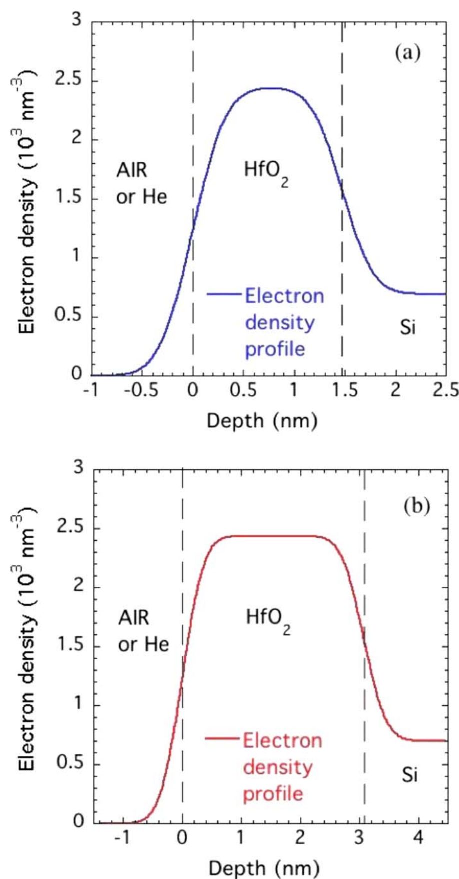

FIG. 3. (Color online) Electron density profiles deduced using the Parratt model of (a) thin and (b) thick ALD HfO_2 films after annealing at 850 °C. The vertical dashed lines indicate the mean positions of the film top surface and the film/substrate interface. The distance between them is defined as the film thickness.

$\mathbf{q_y}$ and $\mathbf{q_z}$ must be measured, respectively, at nonzero $\mathbf{q_z}$ and nonzero $\mathbf{q_y}$ because the internal structural information is masked by occlusion by the sample at $\mathbf{q_z}=\mathbf{0}$ and by the specular reflectivity profile at $\mathbf{q_y}=\mathbf{0}$.

The x-ray undulator/Ge(111) monochromator combination was set to use an x-ray energy of 7.349 keV, corresponding to a wavelength λ of 0.1687 nm. This energy was high enough to penetrate the HfO_2 film thickness in grazing-incidence geometry but was safely below the Hf L_{III} x-ray absorption edge at 9.561 keV. A two-dimensional (2D) MAR345 charge-coupled device detector was used with a 2048×2048 pixel array and 79×79 μm^2 pixel size. A sample-to-detector distance of 1895 mm was used, and for an incident beam position on the detector in pixel coordinates of (1012, 1675), the maximum accessible Q for GISAXS studies was found to be ≈ 2 nm^{-1}. For all GISAXS measurements, a complete 2D image of the scattering was obtained within a few seconds. It was important to stop the data collection when even a few detector pixels became saturated in order to maintain the intensity calibration between different measurements. For each sample, 2D GISAXS data sets were collected for incidence angles, here denoted as θ_i, in the range $0.15° < \theta_i < 0.45°$. These data sets were inspected and compared across different samples in order to determine the optimum configuration for carrying out extended data analyses. It was found that the GISAXS data sets with $\theta_i=0.35°$ provided the best compromise between scattering intensity (higher for low θ_i) and minimal distortions due to refraction effects at grazing incidence (better for high θ_i). While some analysis of GISAXS data at other θ_i values was made to determine the location of the scattering features (see below), all of the main GISAXS results presented in this paper have been derived from the analysis of the GISAXS runs taken with $\theta_i=0.35°$.

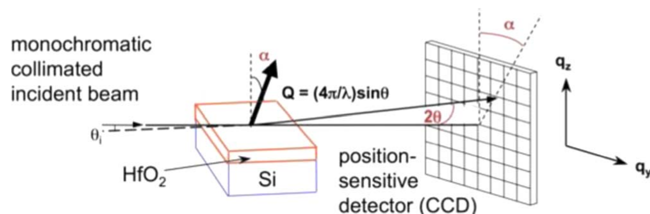

FIG. 4. (Color online) Schematic of GISAXS measurement geometry.

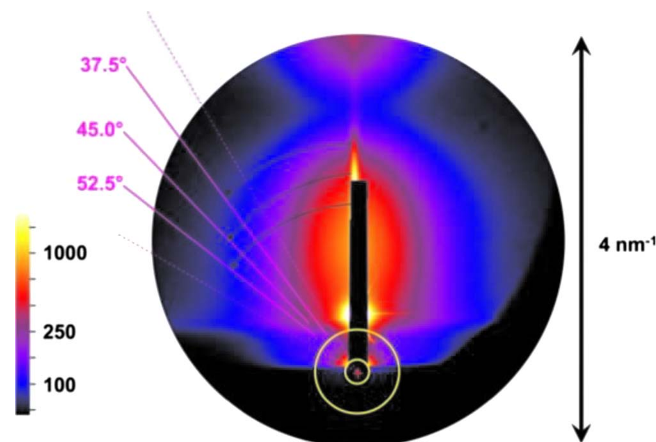

FIG. 5. (Color online) Typical 2D GISAXS data for an as-deposited ALD HfO_2 showing the sectors used for data analysis. Scales are given for the Q-range across the detector and for the measured intensity (using a logarithmic color scale).

Figure 5 shows how the GISAXS data were sector averaged to produce one-dimensional (1D) data sets for model fitting purposes. The prominent feature around the beam stop is mainly scattering from the surface roughness of the film and can be correlated with the results from the reflectivity measurements. GISAXS intensity arising from the true internal structure of the film is given by the much weaker scattering further away from the beam stop. To analyze these data, the 2D data were sector averaged in three 15° wide overlapping sectors as shown. The sectors were centered on azimuthal angle α with respect to the normal direction to the substrate plane, as given by $\alpha=37.5°$, 45°, and 52.5°. The sectors were defined on either side of the substrate plane normal but are only shown on one side here. Sector averaging was used rather than taking orthogonal line cuts to interrogate the scattering intensity variation with respect to $\mathbf{q_y}$ and $\mathbf{q_z}$ directly due to the inherently weak scattering associated with these high density HfO_2 films.

The sector-averaging approach has the disadvantage that it complicates refraction and reflection corrections for x rays penetrating the film surface in grazing incidence geometry, then exiting the film surface after scattering and/or partial

Author complimentary copy. Redistribution subject to AIP license or copyright, see http://jap.aip.org/jap/copyright.jsp

reflection at the film/substrate interface. For $\alpha=0°$ the external incident (θ_i) and outgoing (θ_f) grazing angles, together with the apparent scattering angle ($\Phi_s=\theta_i+\theta_f$), are easily transformed into their internal equivalents within the film (θ_{ii}, θ_{ff}, and $\Phi_{ss}=\theta_{ii}+\theta_{ff}$) by relations such as $\theta_{ii}^2=\theta_i^2-\theta_c^2$. For a finite α, the outgoing grazing angles are changed into θ_2 [$=\theta_f\cos(\alpha)$] and θ_{22} ($=\theta_{ff}\cos(\alpha)$) where $\theta_{22}^2=\theta_2^2-\theta_c^2$. A full description of the transformations among these terms for an arbitrary azimuthal angle α is given elsewhere.[19] Here we simply summarize that these refraction effects transform both the direction and magnitude of $\mathbf{Q}(=\mathbf{q_y}+\mathbf{q_z})$, measured externally to the sample, into $\mathbf{Q}'(=\mathbf{q_y}'+\mathbf{q_z}')$, actually applicable to the scattering inside the sample, where $\mathbf{q_y}'=\mathbf{q_y}$ (i.e., the component of $\mathbf{Q}$ parallel to the substrate is not changed).

For the experimentally determined critical angle θ_c ($\theta_c=0.22°\pm0.05°$ for 7.35 keV x rays) and for $\theta_i=0.35°$, the correction to $\mathbf{q_z}$ and $\mathbf{Q}$ is small, i.e., no more than 7% over the range of interest, and only 3% to 4% for the scattering at high Q associated with the fine primary feature size discussed below. The results derived from this sector-averaged analysis were compared with those from a more direct $\mathbf{q_y}$, $\mathbf{q_z}$ analysis where the scattering was sufficiently strong to permit this. Although full refraction corrections were made in the latter case, using the program by Lee,[20] the in-plane and out-of-plane feature sizes agreed well with those resolved from the sector-averaged analysis without correction.

It is important to determine the location of the scattering features observed by GISAXS, i.e., to distinguish between surface roughness features and internal film microstructure. Two parameters of interest in this connection are the maximum and mean penetration depths associated with the GISAXS data. The maximum penetration depth ξ_{max} is given by[19]

$$\xi_{max}=L_S/\{\cot\theta_{ii}+\cot\theta_{22}\}, \tag{1}$$

where L_S is the sample length along the beam ($\approx$40 mm for the present samples). Given the incidence, critical, and scattered angles relevant to the present experiments, it is clear that ξ_{max} is of order 150 μm, and hence several orders of magnitude greater than the sample A or B film thicknesses. However, the attenuation of the x-ray path through the HfO_2 at grazing incidence reduces the actual mean penetration depth ξ_{mean} to a much lower value given by

$$\xi_{mean}=\xi_{max}(1/\Sigma_T L_S)\{2+\Sigma_T L_S-(2/T_S)\}, \tag{2a}$$

where

$$T_s=2\{\exp(-\Sigma_T L_S)+\Sigma_T L_S-1\}/(\Sigma_T L_S)^2 \tag{2b}$$

and Σ_T is the total x-ray linear attenuation constant for HfO_2 (1.54×10^5 m^{-1} at this x-ray energy). Substitution of appropriate values into the above equations yields a ratio given by $\xi_{mean}/\xi_{max}\approx1/3000$, which implies that $\xi_{mean}\approx50$ nm, which is still more than an order of magnitude greater than our HfO_2 film thicknesses. This means that unlike other GISAXS studies of thicker structured or porous films, including HfO_2 films for catalysis applications,[21] GISAXS studies of ALD HfO_2 high-κ dielectric films thin enough to be of technological interest are essentially confined to studies of features in a near-surface geometry.

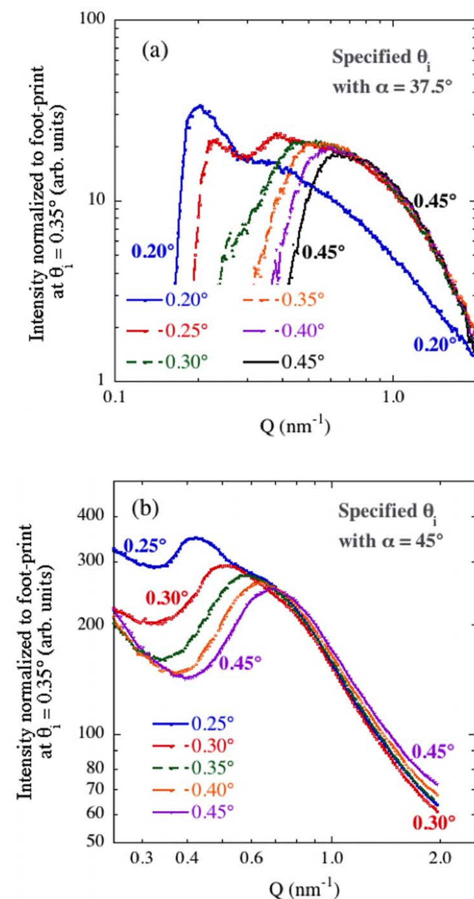

FIG. 6. (Color online) ALD HfO_2 thick film, as-grown sector-averaged GISAXS data for specified grazing incidence angle θ_i: (a) above and below the critical angle θ_c for 1D sector-averaged data at $\alpha=37.5°$; (b) above θ_c for 1D sector-averaged data at $\alpha=45°$.

Despite the thinness of the ALD HfO_2 films, it is possible by varying the grazing incidence angle θ_i to distinguish the scattering from structures within the films from features solely on the top surface (i.e., surface roughness). Figure 6(a) shows 1D sector-averaged GISAXS data from the as-deposited thick film (sample D) at various θ_i values, each for the sector shown in Fig. 5 with $\alpha=37.5°$, but with the scattering intensities normalized to the beam footprint on the sample for $\theta_i=0.35°$. Except for the low-Q cutoff defined by the geometry, the intensity per unit film area for the GISAXS data of interest ($Q>\approx0.4$ nm^{-1}) increases slightly as θ_i is increased above 0.25°. However, as θ_i is reduced below θ_c (as shown here in the data for $\theta_i=020°$) the GISAXS intensity per unit film area decreases significantly. This is clear evidence that the main GISAXS data of interest arise from structure within the film rather than on its top surface. Furthermore, in Fig. 6(b), GISAXS 1D sector-averaged data obtained using longer counting times are plotted from the same sample for $\alpha=45°$ at various $\theta_i>\theta_c$. The intensity per unit film area at high Q increases as θ_i is increased with the greatest increase at the highest Q values. This strongly suggests structures that either permeate the whole film thickness or, in the case of the finest features, are likely located toward the bottom of the film near the substrate.

Author complimentary copy. Redistribution subject to AIP license or copyright, see http://jap.aip.org/jap/copyright.jsp

Returning to Fig. 6(a), the GISAXS data at low Q values increase in intensity per unit film area as θ_i is decreased below θ_c, indicating that this scattering is from surface features and can be associated with the prominent scattering behind the beam stop seen in Fig. 5, which was also found to remain in the 2D detector images for $\theta_i < \theta_c$. A basic analysis of this feature along the $\mathbf{q_y}$ direction using the available SAXS and GISAXS analysis packages[15,19] indicates a surface feature mean dimension parallel to the plane of the film between 8 and 9 nm, consistent with the larger features discussed below.

A complete quantitative analysis of all the GISAXS data from first principles would require a full model treatment based on the distorted wave Born approximation (DWBA)[7,8] and the extraction of 1D data in narrow line cuts of the GISAXS detector 2D data. In practice, this requires both a very accurate sample alignment and sufficiently strong sample scattering to provide acceptable 1D data statistics. However, scattering from the internal structure of our HfO_2 thin films was very weak. Care was taken to ensure that the GISAXS data were measured under identical geometrical conditions with $\theta_i = 0.35°$, and the results presented are based on comparison between the samples and the reference samples C and D. Thus, a full DWBA treatment was not attempted here; however, while lacking some of the refinements and corrections possible with the DWBA method, we were able to produce meaningful results through the use of sector averaging, comparisons of the data between different scattering geometries, and selection of a carefully designed set of samples.

Figure 7(a) shows a typical 1D sector-averaged GISAXS data for $\theta_i = 0.35°$, corresponding to the sectors associated with mean values of $\alpha = 37.5°$, 45°, and 52.5°. The entropy maximization routine MaxEnt was used to extract apparent volume-weighted feature size distributions from these data, as described elsewhere.[22] (MaxEnt has become widely used in recent years to extract size distributions from small-angle scattering data.) The resulting size distributions are shown in Fig. 7(b) where it can be seen that there is a bimodal distribution of scattering features. The dominant (in volume fraction) scattering features are about 2 nm in mean size, and their apparent size distribution does not change appreciably with α; we denote these as the "primary" features. Larger scattering features, 6–8 nm in apparent size, are also present, but with a much smaller volume fraction; we denote these as the "large" features.

The large features appear to get larger with increasing α ($\mathbf{Q}$ direction closer to the plane of the film). Using simple geometrical arguments, this can be interpreted as indicating that they have extended dimensions in the plane of the film. Approximating the large features as oblate spheroids, it was possible to extract their mean in-plane dimension D_Y from the apparent mean dimension D_α measured for each sector in α. By reason of the arguments advanced above for the location of the features giving rise to the GISAXS intensity, it was assumed that the features extend through the film thickness. Thus, the mean out-of-plane dimension D_Z should be the same as the film thickness and for a spheroid

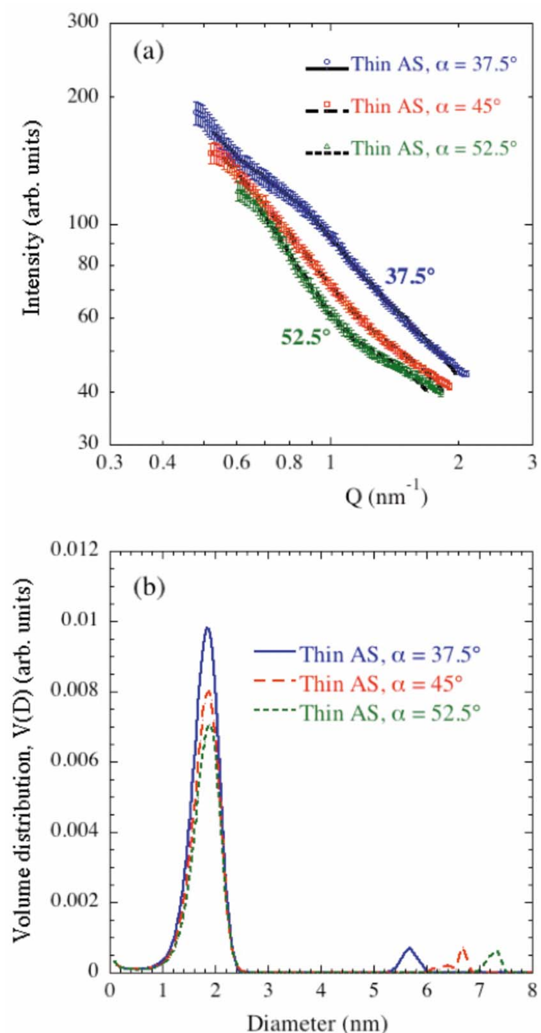

FIG. 7. (Color online) ALD HfO_2 thin film, as-deposited (AS): (a) sector-averaged GISAXS data with MaxEnt fits for sectors at $\alpha = 37.5°$, 45°, and 52.5°; (b) corresponding MaxEnt feature size distributions. Note that the apparent size of the larger features increases with α, indicating their extended size parallel to the substrate.

$$D_Y = \frac{\sqrt{D_\alpha^2 - D_Z^2 \cos^2 \alpha}}{\sin \alpha}. \tag{3}$$

For each of the samples studied, this equation produced a single real result for D_Y for the large features when applied to any of the three 1D sector-averaged data sets defined above in terms of α. The mean in-plane dimension of the large features D_Y was found to be between 8 and 9 nm. Equation (3) was also used for the small primary features. In the case of the thin films, a single real result was again obtained for each film with D_Y for the primary features, comparable to the apparent mean dimension D_α measured in all three sectors. However, in the case of the thick films, it was found that the numerator of Eq. (3) did not generally give a real result for the primary features when D_Z was set equal to the full film thickness. In these cases, the value of D_Z was iteratively reduced by trial until a consistent result for D_Y could be obtained for the primary features derived from the three sector-averaged data sets. In this way, it was established that the small primary features are globular in shape

Author complimentary copy. Redistribution subject to AIP license or copyright, see http://jap.aip.org/jap/copyright.jsp

and, in the case of the thick films, they do not extend through the whole film thickness. The large features do extend through the whole film thickness in both the thin and thick films, but they have extended dimensions in the plane of the film regardless of film thickness.

Results for the three sector-averaged 1D data sets were compared for consistency in derived feature size and then combined as discussed above. Individually, their scattering intensities and derived feature volume fractions were compared with those for the corresponding sectors derived from the GISAXS data for the as-grown (unannealed) films. It is these comparisons that form the basis of many of the GISAXS-derived results presented below. Thus, broadly, the GISAXS microstructure information is based on the data in a sector between $\alpha=30°$ and $60°$ and at sufficient Q values such that the data are affected neither by specular reflection nor by sample surface occlusion.

III. RESULTS AND DISCUSSION

ALD HfO_2 films, if optimally grown, are planar, initially amorphous, and almost fully dense (90%–95%).[9] Furthermore, time-of-flight secondary ion mass spectrometry (TOF-SIMS) suggests that the films must be smooth to within a small fraction of the mean film thickness. This is because TOF-SIMS data indicate that even the thinnest such films nucleate and grow linearly and uniformly over the substrate surface.[9] Since GISAXS scattering contrast results from local areas with atomic number (Z) gradients, one would not expect extensive scattering from such ideal samples. Thus, the scattering we report in this paper is due to imperfections in the film, e.g., voids, and interfacial roughness (from the HfO_2/Si and HfO_2/air interfaces). Further, inasmuch as the films are relatively dense to begin with, the scattering volumes are small, no greater than about 5%–10%, and may be significantly less. Thus, changes in the overall film density indicated by a decrease in the volume fraction of scatterers represent a change to a small percentage of the film and therefore push the limits of detectability even for GISAXS. Even though they may profoundly affect electrical behavior, such small changes would not likely be observable by any other technique. Meanwhile, the XRR data indicate that uniform parallel-sided films are maintained throughout all of the annealing studies reported here, and the XRR measurements do not have sufficient sensitivity to detect systematically any significant reduction in the solid HfO_2 electron density in these thin ALD films. While the XRR electron density profile of each ALD film may be used in principle to calculate its overall average density, the result is a complex function of interfacial diffuseness, surface roughness, and internal porosity, only the last of which is expected to correlate with GISAXS data from the film internal structure. Thus, in the results that follow, we present the GISAXS feature sizes with their relative volume fractions and the XRR film thicknesses with their associated roughness/diffuseness dimensions, as these provide the most sensitive measures of the changes in the films as a function of the annealing temperature.

HfO_2 film thickness (τ_{refl}) and the interfacial roughness/

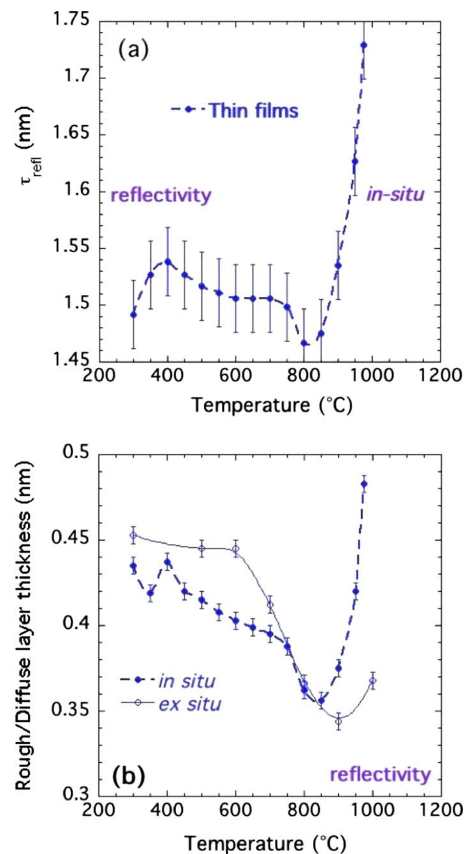

FIG. 8. (Color online) XRR measurements of sample A as a function of annealing temperature: (a) film thickness and (b) interfacial roughness/diffuseness dimension. Also shown in (b) are roughness/diffuseness measurements for samples C, E, G, I, K, M, and O for comparison.

diffuseness dimension σ_R defined earlier are plotted for samples A and B in Figs. 8 and 9 as a function of annealing temperature. For the *in situ* samples A and B, the same coupon, as well as the same spot on the coupon, was used for the entire annealing experiment on the thin (A) and thick (B) films. In general, the mean roughness/diffuseness dimension tends to mirror the HfO_2 film thickness. The variations in thickness due to annealing are small and would be in the noise for other commonly used thickness determination (e.g., ellipsometric, electron microscopy, or capacitance-voltage) measurements. The total range of variation for sample A is 0.26 nm (film thickness) and 0.13 nm (roughness/diffuseness), whereas for sample B it is 0.11 nm (film thickness) and 0.08 nm (roughness/diffuseness). The as-grown (300 °C) mean roughness/diffuseness dimension is 0.44 nm for sample A and 0.42 nm for sample B, each with estimated standard deviation uncertainties of ± 0.005 nm; these roughness/diffuseness measurements are on the low end of interlayer thicknesses for ALD oxides grown on chemically oxidized Si.[23,24] Much of the diffuse thickness can be attributed to the Si/HfO_2 interface, but the slightly larger value for the thinner sample (A) suggests an additional top surface roughness component. Clearly, top surface roughness components are indicated for both film thicknesses if the full roughness/diffuseness layer thicknesses are taken as $\{2\sigma_R(2 \ln 2)^{0.5}\}$.

Figures 8(a) and 9(a) show that for both thin and thick

Author complimentary copy. Redistribution subject to AIP license or copyright, see http://jap.aip.org/jap/copyright.jsp

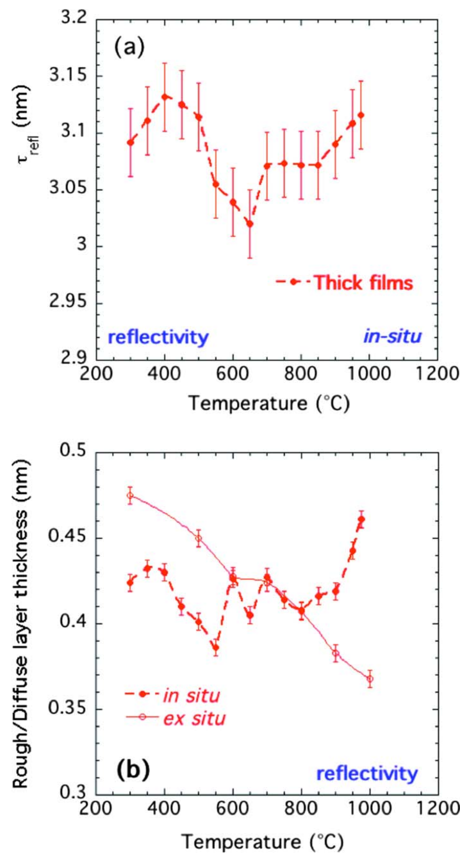

FIG. 9. (Color online) XRR measurements of sample B as a function of temperature: (a) film thickness and (b) interfacial roughness/diffuseness dimension. Also shown in (b) are roughness/diffuseness measurements for samples D, F, H, J, L, N, and P for comparison.

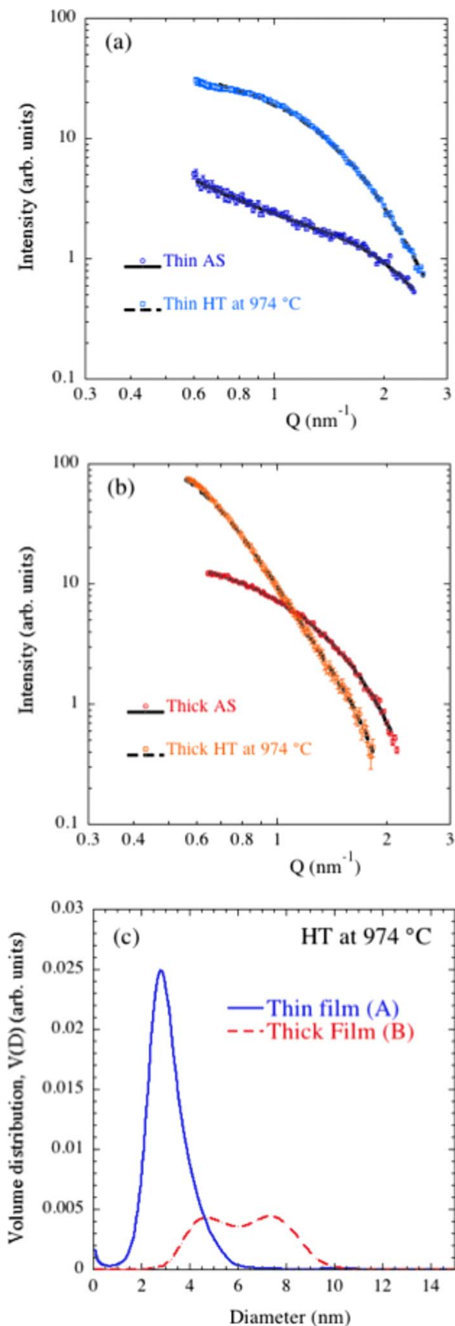

FIG. 10. (Color online) As-grown (AS) and *in situ* annealed at 974 °C (HT) sector-averaged GISAXS data with MaxEnt fits for sectors at $\alpha=45°$ for (a) thin and (b) thick films and (c) the corresponding MaxEnt size distributions. Vertical bars in (a) and (b) represent the computed standard deviation uncertainties in GISAXS data.

films, the film thickness tends to decrease with increasing annealing temperature, reaching a minimum at 800 °C for the thin film and 650 °C for the thick film. At higher annealing temperatures, the thickness increases more substantially for the thin film. Annealing the mostly amorphous HfO_2 films (some crystal nuclei have been observed in as-grown films[25]) at temperatures above 300 °C (the growth temperature) results in nucleation and growth of monoclinic, tetragonal, or orthorhombic HfO_2 phases. The extent of crystallization is significant after 500 °C anneals[25] and the films are entirely crystallized after anneals between 600 °C[26] and 900 °C.[25]

Also plotted in Figs. 8(b) and 9(b) are variations in the roughness/diffuseness dimension with annealing temperature for samples E–P. Comparison of the *in situ* annealed (samples A and B) and *ex situ* annealed (samples E–P) results reveals similar trends for annealing temperatures up to 800 °C, but only the roughness/diffuseness dimension for the *in situ* samples shows a marked increase after higher temperature anneals. For the thick films the *in situ* roughness/diffuseness dimension shows a somewhat complex behavior for annealing temperatures above 650 °C, while that for *ex situ* samples shows a monotonic decrease for temperatures up to 1000 °C, the highest annealing temperature. For both film thicknesses, the roughness/diffuseness dimension at the end of the *in situ* study is significantly larger than for the *ex situ* samples, which only saw one annealing cycle.

GISAXS data for *in situ* samples A and B are shown in Fig. 10, as-grown (300 °C) and after the 974 °C anneal. The 974 °C anneal was the last of many excursions at various temperatures between 350 and 974 °C, all on the same sample coupon. The highest temperature excursions represent conditions normally encountered by fabricated high-κ dielectric ALD films in subsequent device processing. Depending on the Q range, one can see a three- to tenfold increase in the scattering intensity for the thin sample (A)

Author complimentary copy. Redistribution subject to AIP license or copyright, see http://jap.aip.org/jap/copyright.jsp

and a more complex change for the thicker sample (B) that may indicate sintering out of the finest features and coarsening of larger ones. In fact, there is a net coarsening in the feature sizes for both films, as can be seen in the size distributions (rather different for thin and thick films) shown in Fig. 10(c), when compared to Fig. 7(b) for the as-grown films. The vertical axes of these two figures are not on the same scale, but the total volume fractions in Fig. 10(c) are significantly increased from those in the corresponding as-grown state by some three and two times, respectively, for thin and thick films. These dramatic effects were not observed for the *ex situ* annealed samples (data not shown) possibly because those samples were annealed only in one heating cycle. The GISAXS data shown in Fig. 10 can be associated with the *in situ* reflectivity results shown in Figs. 8 and 9 for the highest temperature (974 °C) anneals. In the case of the thin film (sample A), the 10% increase in the XRR film thickness at the highest temperatures would be consistent with the significant increase in the porosity measured by GISAXS (perhaps from 5% to 15% in absolute terms). Certainly, the XRR data could be fitted using the Parratt model with a 10% reduction in the HfO_2 electron density. However, even in this case, the XRR data indicated a planar uniform geometry with no evidence of significant disruption in the film integrity.

The volume fractions of primary (small) and large size scattering features in the *ex situ* samples E–P are plotted as a function of annealing temperature in Fig. 11. The data in Fig. 11(a) is normalized to the volume fraction of scattering features in the as-grown (300 °C) thin and thick films, respectively. In Fig. 11(b), all of the data are normalized to the volume fraction of scattering features in the as-grown thin film. Thus, the data of Fig. 11(a) are effectively normalized to unit film *area*, while the data in Fig. 11(b) are normalized to film *volume*. One can therefore see that the thick film has only half of the small scattering features compared to the thin film on a volume basis and therefore must consist of a two layer structure in which the small scattering features appear to be confined to the initial thin layer and are present to a much lesser extent in the upper half of the thick film layer. Direct evidence supporting this interpretation can be seen in Fig. 6(b), where the GISAXS intensity at high Q associated with fine features is greatest for the steepest grazing incidence angle (largest θ_i). This strongly suggests that the small scattering features are associated with film coalescence, which is known to occur at about 2 nm of ALD HfO_2 deposition.[9] This point is further supported by applying Eq. (3), as described earlier, to determine the in-plane and out-of-plane dimensions of the primary features. We find that the small primary features only extend through about half the thickness of the thicker films. The GISAXS data in Fig. 11 can be associated with the *ex situ* reflectivity results shown in Figs. 8 and 9. In contrast to the *in situ* results, there is a slight reduction in the volume fraction of the scattering features here. Note that these volume fractions assume that the scattering features are voids.

Figure 12 is a plot of scattering feature size as a function of annealing temperature for the *ex situ* samples C–P. Note that all samples show a bimodal distribution of scattering features and that the size of these features does not change appreciably with annealing temperature, except for the case of the small scattering features in the thin films. The large size scattering features are slightly smaller for the thick film

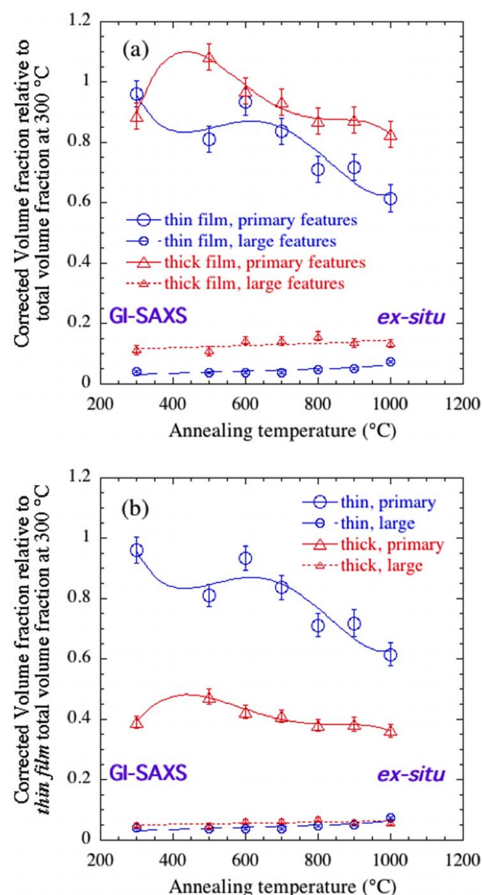

FIG. 11. (Color online) Feature (void) volume fractions in ALD HfO_2 films vs *ex situ* one-time temperature cycling to the indicated annealing temperature relative to the total porosities for (a) the corresponding film at 300 °C and (b) the thin film at 300 °C. Vertical bars represent the estimated standard deviation uncertainties.

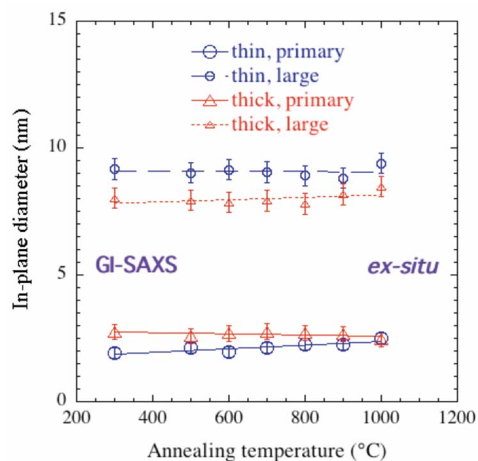

FIG. 12. (Color online) Derived feature (void) in-plane diameters in ALD HfO_2 films vs *ex situ* annealing temperature. The in-plane diameters have been obtained using Eq. (3) applied to the sector-averaged GISAXS data in the sectors at $\alpha = 37.5°$, 45°, and 52.5° for each sample. Vertical bars represent the estimated standard deviation uncertainties.

Author complimentary copy. Redistribution subject to AIP license or copyright, see http://jap.aip.org/jap/copyright.jsp

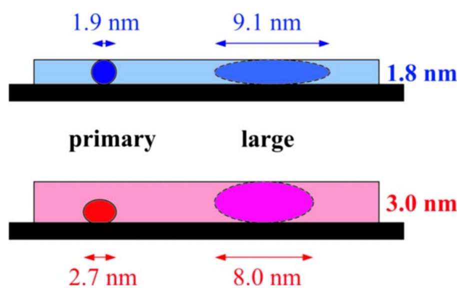

FIG. 13. (Color online) Schematics of proposed morphologies for primary (fine) and large scattering features.

than for the thin film, whereas the small sized scattering features are about the same size within the experimental uncertainties for both films. In-plane feature dimensions do not change with annealing, although volume fraction does.

Interpretation of film nanostructure

We now interpret our experimental results with the goal of arriving at an accurate picture of the nanostructure of ALD HfO_2 films and how it evolves with annealing. The as-grown films are largely amorphous and 90%–95% dense.[9] Most of the scattering we observe is from whatever structure is associated with 5%–10% of empty space. We further know that the majority of the scattering is from structures with a characteristic size of about 2 nm, and that these features are predominant in the thinner films and in the bottom part of the thicker films. We also observe relatively weak scattering from structures whose characteristic apparent length is 6–8 nm in the 1D sector-averaged GISAXS data analyzed, but for which the mean in-plane dimension is derived to be between 8 and 9 nm. These features exist throughout the film thickness. Ho *et al.*[25] observed x-ray coherence lengths in the range of 8 nm to ≈ 10 nm upon annealing HfO_2 films.

The in-plane dimensions of the primary and large scattering features are plotted in Fig. 12 for both thin and thick films. Primary features (2 nm) are characteristic of ALD film nuclei,[27,28] and this feature is also related to film coalescence. The fact that the feature seems to disappear in the upper layer of the thicker films, i.e., after about 1.5 nm of growth, suggests that the feature results from HfO_2 nucleation primarily on SiO_2 [chemically oxidized Si[9]]; once HfO_2 nucleation primarily takes place on HfO_2, i.e., when the film has coalesced and no further Si–OH sites are available for nucleation, the feature disappears. Thus, the small features are most likely the occasional "missing" nuclei of HfO_2 but may also be due to the way the nuclei knit together before coalescence, as opposed to after coalescence. If ALD growth could occur at a full monolayer per cycle, one would not expect to see these features, which we believe are a remnant of the submonolayer patchwork growth.[29]

The small primary and large secondary scattering features are drawn schematically in Fig. 13. The large features are drawn in pale color, as these may not be voids but simply dense elements of film bounded by subnanometer thick boundaries not visible to GISAXS. Since the effective scattering contrast would then be much reduced, the volume fractions may be much larger than indicated in Fig. 11, and this morphology may even extend throughout the entire film volume. As stated earlier, the prominent diffuse scattering feature behind the beam stop in the 2D GISAXS data appears to be associated with the large feature mean size in the plane of the film, and this may indicate that the large feature morphology is also responsible for the top surface film roughness.

Finally, Figs. 8(b), 9(b), and 11 indicate that the *ex situ* samples show evidence of densification upon annealing, in that both the mean roughness/diffuseness dimension [Figs. 8(b) and 9(b)] and the relative volume fraction of the primary scattering features (Fig. 11) decrease with higher annealing temperature., Based on electrical property measurements and transmission electron microscopy analysis, earlier work[30] suggested that the ALD HfO_2 films were 100% dense. Our new results are based on a far more sensitive probe of the structure than has been available previously and indicate that the as-grown films are not fully dense. Their density increases as a result of annealing, but it is unlikely that it attains 100% because scattering persists even after the highest temperature anneals. Other techniques, such as positron annihilation analysis, might be useful in measuring the degree of porosity that remains after annealing. Meanwhile, the *in situ* samples demonstrate that prolonged exposure to the highest annealing temperatures can reverse densification and, instead, coarsen the film morphology while increasing both the porosity and the overall film thickness. Future studies should explore how far such high temperature cycling can continue before the films are disrupted and the high-κ dielectric integrity is destroyed.

IV. CONCLUSIONS

A series of ALD HfO_2 high-κ dielectric films has been studied by a combination of XRR and GISAXS measurements. By using these techniques together, it has been shown how the surface, interfaces, and internal structure of thin high-κ dielectric films can be characterized with unprecedented sensitivity. Although the films are dense, an internal film structure is shown to exist, believed to comprise primarily small "missing island" porosity close to the substrate. Following coalescence, further film thickness buildup no longer contains such voids. Occasional larger features also appear to be present. If voids, these are extremely rare; however, these features may also be indicative of a widespread modulation in the film density that pervades the entire film volume and contributes to surface roughness.

The main effects of single, brief, high-temperature excursions to >900 °C are subtle but significant, namely, to anneal out some of the fine voids and to reduce the mean roughness/diffuseness dimension of the film. These changes are indicative of densification. However, the annealing behavior at temperatures between 650 and 800 °C (depending on the film thickness) can be quite different for repeated high-temperature cycling, compared to a single brief high-temperature excursion. Particularly for thin, just-coalesced films, XRR indicates marked increases in the film thickness and in the mean roughness/diffuseness dimension for repeated or extended temperature cycling to the highest tem-

Author complimentary copy. Redistribution subject to AIP license or copyright, see http://jap.aip.org/jap/copyright.jsp

peratures explored. GISAXS also shows an increase, rather than a reduction, in the void microstructure under these conditions. Although the films remained planar, the measured effects of repeated high-temperature cycling may be a precursor to a loss of film integrity. Overall, using a combination of XRR and GISAXS, we have measured nanoscale structural changes in ALD HfO_2 films with unprecedented sensitivity. These changes have implications for HfO_2 gate dielectric performance after the high temperature thermal budget cycles they will be exposed to during processing.

ACKNOWLEDGMENTS

We thank Xuefa Li and Jin Wang of X-ray Operations and Research, Advanced Photon Source, Argonne National Laboratory, IL for assistance with the GISAXS measurements and for valuable discussions. Use of the Advanced Photon Source was supported by the U.S. Department of Energy, Office of Science, Office of Basic Energy Sciences, under Contract No. DE-AC02-06CH11357. Use of the National Synchrotron Light Source, Brookhaven National Laboratory, was supported by the U.S. Department of Energy, Office of Science, Office of Basic Energy Sciences, under Contract No. DE-AC02-98CH1088.

[1]M. L. M. Ritala, in *Handbook of Thin Film Materials: Deposition and Processing of Thin Films*, edited by H. S. Nalwa (Academic, New York, 2002), Vol. 1.
[2]G. D. Wilk, R. M. Wallace, and J. M. Anthony, J. Appl. Phys. **89**, 5243 (2001).
[3]H. Kim, J. Vac. Sci. Technol. B **21**, 2231 (2003).
[4]M. L. Green, E. P. Gusev, R. Degraeve, and E. L. Garfunkel, J. Appl. Phys. **90**, 2057 (2001).
[5]M. L. Green, A. J. Allen, X. Li, J. Wang, J. Ilavsky, A. Delabie, R. L. Puurunen, and B. Brijs, Appl. Phys. Lett. **88**, 032907 (2006).
[6]S. Stemmer, Y. L. Li, B. Foran, P. S. Lysaght, S. K. Streiffer, P. Fuoss, and S. Seifert, Appl. Phys. Lett. **83**, 3141 (2003).
[7]R. Lazzari, F. Leroy, and G. Renaud, Phys. Rev. B **76**, 125411 (2007).
[8]M. Rauscher, T. Salditt, and H. Spohn, Phys. Rev. B **52**, 16855 (1995).
[9]M. L. Green, M. Y. Ho, B. Busch, G. D. Wilk, T. Sorsch, T. Conard, B. Brijs, W. Vandervorst, P. I. Raisanen, D. Muller, M. Bude, and J. Grazul, J. Appl. Phys. **92**, 7168 (2002).
[10]J. L. Jordan-Sweet, C. Detavernier, C. Lavoie, P. M. Mooney, and M. F. Toney, Nucl. Instrum. Methods Phys. Res. B **241**, 247 (2005).
[11]J. L. Jordan-Sweet, IBM J. Res. Dev. **44**, 457 (2000).
[12]Certain commercial materials and equipment are identified in this paper only to adequately specify the experimental procedure. In no case does such identification imply recommendation by NIST nor does it imply that the material or equipment identified is necessarily the best available for this purpose.
[13]L. G. Parratt, Phys. Rev. **95**, 359 (1954).
[14]A. Nelson, J. Appl. Crystallogr. **39**, 273 (2006).
[15]J. Ilavsky and P. R. Jemian, J. Appl. Crystallogr. **42**, 347 (2009).
[16]D. L. Windt, IMD 4.1.1, available at http://cletus.phys.columbia.edu/windt/idl, 2000.
[17]A. R. Sandy, L. B. Lurio, S. G. J. Mochrie, A. Malik, G. B. Stephenson, J.-F. Pelletier, and M. Sutton, J. Synchrotron Radiat. **6**, 1174 (1999).
[18]X. Li, S. Narayanan, M. Sprung, A. R. Sandy, D. R. Lee, and J. Wang, AIP Conf. Proc. **879**, 1387 (2007).
[19]A. Naudon and D. Thiaudiere, J. Appl. Crystallogr. **30**, 822 (1997).
[20]B. Lee, GISAXS toolkit program, available at blee@aps.anl.gov, 2005.
[21]J. C. Hackley, T. Gougousi, and J. D. Demaree, J. Appl. Phys. **102**, 034101 (2007).
[22]J. A. Potton, G. J. Daniell, and B. D. Rainford, J. Appl. Crystallogr. **21**, 663 (1988).
[23]G. D. Wilk and D. A. Muller, Appl. Phys. Lett. **83**, 3984 (2003).
[24]P. S. Lysaght, J. Barnett, G. I. Bersuker, J. C. Woicik, D. A. Fischer, B. Foran, H.-H. Tseng, and R. Jammy, J. Appl. Phys. **101**, 024105 (2007).
[25]M.-Y. Ho, H. Gong, G. D. Wilk, B. W. Busch, M. L. Green, P. M. Voyles, D. A. Muller, M. Bude, W. H. Lin, A. See, M. E. Loomans, S. K. Lahiri, and P. I. Raisanen, J. Appl. Phys. **93**, 1477 (2003).
[26]H. Kim, P. C. McIntyre, and K. C. Saraswat, Appl. Phys. Lett. **82**, 106 (2003).
[27]W. F. A. Besling, E. Young, T. Conard, C. Zhao, R. Carter, W. Vandervorst, M. Caymax, S. De Gendt, M. Heyns, J. Maes, M. Tuominen, and S. Haukka, J. Non-Cryst. Solids **303**, 123 (2002).
[28]E. P. Gusev, C. Cabral, M. Copel, C. D'Emic, and M. Gribelyuk, Microelectron. Eng. **69**, 145 (2003).
[29]H. S. Chang, H. Hwang, M.-H. Cho, and D. W. Moon, Appl. Phys. Lett. **86**, 031906 (2005).
[30]R. L. Puurunen, A. Delabie, S. Van Elshocht, M. Caymax, M. L. Green, B. Brijs, O. Richard, H. Bender, T. Conard, I. Hoflijk, W. Vandervorst, D. Hellin, D. Vanhaeren, C. Zhao, S. De Gendt, and M. Heyns, Appl. Phys. Lett. **86**, 073116 (2005).

Author complimentary copy. Redistribution subject to AIP license or copyright, see http://jap.aip.org/jap/copyright.jsp